

Cite this: *Chem. Sci.*, 2017, **8**, 437

## Achievement of visible-light-driven Z-scheme overall water splitting using barium-modified $Ta_3N_5$ as a $H_2$ -evolving photocatalyst†

Yu Qi,<sup>a,b</sup> Shanshan Chen,<sup>a</sup> Mingrun Li,<sup>a</sup> Qian Ding,<sup>a,b</sup> Zheng Li,<sup>a,b</sup> Junyan Cui,<sup>a,c</sup> Beibei Dong,<sup>a,b</sup> Fuxiang Zhang<sup>\*a</sup> and Can Li<sup>\*a</sup>

$Ta_3N_5$  is one of the most promising photocatalyst candidates for solar water splitting, but it still remains challenging to achieve overall water splitting via  $Ta_3N_5$ -based photocatalysts regardless of whether it uses a one step or two step method. Here we will address the relatively poor photocatalytic proton reduction of  $Ta_3N_5$  with an effort for the promotion of charge separation via barium modification. One-pot nitridation of barium nitrate-impregnated  $Ta_2O_5$  precursor was adopted here for the synthesis of  $Ta_3N_5$  accompanied with the creation of a  $Ta_3N_5/BaTaO_2N$  heterostructure and surface passivation. Due to the synergistic effect of the improved interfacial charge separation and the decreased defect density, the photocatalytic  $H_2$  evolution rate of barium-modified  $Ta_3N_5$  is effectively promoted. Encouraged by this, a visible-light-driven Z-scheme overall water splitting system was successfully constructed by using the barium-modified  $Ta_3N_5$  as a  $H_2$ -evolving photocatalyst, together with a  $PtO_x/WO_3$  and  $IO_3^-/I^-$  pair as an  $O_2$ -evolving photocatalyst and a redox mediator, respectively.

Received 22nd June 2016  
Accepted 18th August 2016

DOI: 10.1039/c6sc02750d  
[www.rsc.org/chemicalscience](http://www.rsc.org/chemicalscience)

## Introduction

Semiconductor-based photocatalytic overall water splitting for hydrogen production is an ideal way to convert solar energy to chemical energy and has inspired extensive interest in the past few decades.<sup>1–5</sup> Towards this, hundreds of semiconductors have been reported for potential solar water splitting, but most of them are only active under UV light irradiation.<sup>6–10</sup> To achieve highly efficient solar-to-chemical energy conversion, overall water splitting on photocatalysts harvesting visible light with longer wavelength is desirable. To date, however, the number of wide visible-light-driven overall water splitting systems, regardless of whether they use a one step or two step method, is limited.<sup>5,11–18</sup>

Tantalum nitride ( $Ta_3N_5$ ), with a theoretical solar-to-hydrogen conversion efficiency of 15.9%, is one of the most promising candidates for solar water splitting, considering its matched band edge positions (conduction band and valence band edges at *ca.* –0.4 V and +1.7 V *vs.* NHE, respectively, at pH = 0), wide visible light harvesting ability (up to 600 nm) and

good photo-stability.<sup>19–37</sup> It was first synthesized in 1973,<sup>38</sup> but was not found to be active for the photocatalytic water splitting reaction until 2002.<sup>19</sup> Afterwards,  $Ta_3N_5$  has been widely investigated for water splitting in terms of particulate photocatalysts<sup>22–25</sup> and photoanodes.<sup>26–31</sup>

The increasing research interest and efforts have greatly promoted the water oxidation performance of  $Ta_3N_5$  for both particulate photocatalyst and photoanode systems. For example, Li *et al.* fabricated a 1D  $Ta_3N_5$  nanorod photoanode to achieve a STH of 1.5%.<sup>30</sup> Liu *et al.* achieved  $Ta_3N_5$  photoanode stability for hours<sup>27</sup> and obtained nearly close to the theoretical photocurrent at a potential of 1.23 V *vs.* RHE under AM 1.5G simulated sunlight.<sup>31</sup> Chen *et al.* reported that the apparent quantum efficiency of the photocatalytic water oxidation activity of the  $Ta_3N_5$ -based particulate photocatalyst can reach 11.3% at 500–600 nm *via* an interface engineering strategy.<sup>24</sup> Compared to the water oxidation, however, the activity of photocatalytic proton reduction from water is much lower or even undetectable in most cases, even though extensive investigations such as forming polymorphic macroporous  $Ta_3N_5$ , reducing the particle size through templates (*i.e.*  $SiO_2$ ,  $C_3N_4$ ) and surface modification have been made.<sup>32–37</sup> As a result of the poor proton reduction ability, Z-scheme overall water splitting using particulate  $Ta_3N_5$  as a  $H_2$ -evolving photocatalyst is still not reported.

Fabricating nanocomposites with another semiconductor to form heterostructures has been extensively adopted for the promotion of photocatalytic performances.<sup>16,39–42</sup> A heterostructure can create external bias through interfacial junctions to spatially separate the photogenerated electrons and holes.

<sup>a</sup>State Key Laboratory of Catalysis, iChEM, Dalian Institute of Chemical Physics, Chinese Academy of Sciences, Dalian National Laboratory for Clean Energy, Dalian, 116023, China. E-mail: fxzhang@dicp.ac.cn; canli@dicp.ac.cn; Web: <http://canli.dicp.ac.cn>

<sup>b</sup>University of Chinese Academy of Sciences, Beijing 100049, China

<sup>c</sup>Key Laboratory of Surface and Interface Chemistry of Jilin Province, College of Chemistry, Jilin University, Changchun 130021, China

† Electronic supplementary information (ESI) available. See DOI: [10.1039/c6sc02750d](https://doi.org/10.1039/c6sc02750d)



However, it should be pointed out that most of the (oxy)nitride photocatalysts are thermally unstable in air, so the fabrication of a heterostructure for (oxy)nitride commonly confronts technical challenges, rendering feasible examples very limited.<sup>16</sup>

In this work, a barium modification strategy is introduced to address the relatively poor photocatalytic proton reduction activity of  $Ta_3N_5$  under visible light irradiation. A simple one-pot nitridation route was adopted for the synthesis of pristine  $Ta_3N_5$  and barium-modified  $Ta_3N_5$ , in which a barium nitrate-impregnated  $Ta_2O_5$  was used as a precursor. It is found that some  $Ba^{2+}$  ions could be doped into  $Ta_3N_5$  to decrease its defect density. On the other hand, excessive  $Ba^{2+}$  ions will produce  $BaTaO_2N$  *in situ* on the surface of  $Ta_3N_5$  to create a  $Ta_3N_5$ / $BaTaO_2N$  heterostructure. As a result, the photogenerated carrier separation efficiency of  $Ta_3N_5$  can be promoted after the barium modification, causing an effectively enhanced  $H_2$  evolution rate in the presence of methanol. Finally, the first example of a visible-light-driven photocatalytic Z-scheme overall water splitting system using the modified  $Ta_3N_5$  as a  $H_2$ -evolving photocatalyst was successfully constructed.

## Experimental

### Materials and reagents

For the preparation of  $Ba(n)$ - $Ta_3N_5$  samples,  $Ta_2O_5$  (99.99%, Amresco Chemical), and  $Ba(NO_3)_2$  (99.5%, Sinopharm Chemical) were used.  $WO_3$  (99.99%, High Purity Chemical) was used as a water oxidation photocatalyst.  $H_2PtCl_6 \cdot 6H_2O$  (99.5%, Sinopharm Chemical) was employed as the precursor for the reduction cocatalyst.  $CH_3OH$  (99.5%, Sinopharm Chemical) and  $NaI$  (99.5%, Guangfu Chemical) were used as sacrificial electron donors.  $La_2O_3$  (99.95%, Sinopharm Chemical) was applied as a pH buffer agent. All chemicals were used as purchased without further purification.

### Preparation of $Ba(n)$ - $Ta_3N_5$ samples

Typically,  $Ta_2O_5$  powder was impregnated in the  $Ba(NO_3)_2$  aqueous solution with a calculated molar ratio of Ba/Ta, and the dried mixture was then annealed in air at 1073 K for 2 h. The as-prepared powder was treated with “one-pot” nitridation under ammonia flow (250 mL min<sup>-1</sup>) at 1223 K for 20 h. The as-obtained samples are correspondingly denoted as  $Ba(n)$ - $Ta_3N_5$ , where “*n*” stands for the molar ratio of Ba/Ta and when *n* = 1 it stands for  $BaTaO_2N$ . As a comparison, the pure phase of  $Ta_3N_5$  and  $BaTaO_2N$  powder was mechanically mixed at a Ba/Ta molar ratio of 0.3, which is denoted as  $Ta_3N_5$ / $BaTaO_2N$  (0.3)-mix.

### Deposition of cocatalysts

0.2 g of the as-obtained sample was dispersed in a calculated amount of  $H_2PtCl_6$  aqueous solution, and sonicated for *ca.* 5 min. After the solution was completely evaporated in a water bath at 353 K, the resulting powder was collected and reduced at 473 K for 1 h under a flow of 5%  $H_2$ /Ar (200 mL min<sup>-1</sup>). As for the deposition of  $PtO_x$  on the surface of  $WO_3$  for water oxidation, typically, 0.3 g of  $WO_3$  was annealed in the air at 773 K for

2 h, and then 0.2 g of the annealed sample was immersed in a calculated amount of  $H_2PtCl_6$  aqueous solution with sonicating for *ca.* 5 min. After complete evaporation in a water bath at 353 K, the resulting powder was collected and annealed in air at 798 K for 0.5 h.

### Electrochemical analysis

For the Mott–Schottky (M–S) measurement,  $Ta_3N_5$  and  $BaTaO_2N$  powder were deposited on FTO conducting glass *via* electro-phoretic deposition (EPD). Typically, the powder samples (50 mg) and iodine (20 mg) were dispersed in acetone solution (50 mL), and continuously sonicated for 10 min. Afterwards, the FTO electrode was immersed, parallel to another FTO electrode, with a distance of about 1 cm. The duration time was 1 min with 20 V and 1 A applied using a potentiostat (ITECH IT6834), and then the prepared electrodes were calcined under an ammonia flow (250 mL min<sup>-1</sup>) at 723 K for 0.5 h.

The M–S measurement was carried out using a Princeton Applied Research PARSTAT 2273, using 0.5 M  $Na_2SO_4$  aqueous solution as electrolyte with a pH value of 8.5 adjusted using NaOH. The frequency was 1 kHz.

### Characterizations of catalysts

XRD measurements were carried out using a Rigaku D/Max-2500/PC powder diffractometer (Cu  $K\alpha$  radiation) with an operating voltage of 40 kV and an operating current of 200 mA. A scan rate of 5° min<sup>-1</sup> was applied in the range of 10–60°. UV-vis diffuse reflectance spectra (DRS) were recorded using a UV-vis spectrophotometer (JASCO V-550) equipped with an integrating sphere, and  $BaSO_4$  powder was used as the reference for the baseline correction. The morphologies and particle sizes were examined using field emission scanning electron microscopy (FESEM; S-5500, Hitachi). High-resolution transmission electron microscopy (HRTEM) images were obtained using a Tecnai G2 F30 S-Twin (FEI Company) with an accelerating voltage of 300 kV. For the time-resolved IR spectroscopic study, the photocatalyst was fixed on a  $CaF_2$  plate at a density of 2 mg cm<sup>-2</sup> and placed in a gas cell evacuated at 10<sup>-5</sup> Torr. The Brunauer–Emmett–Teller (BET) surface area was measured at 77 K using a Micromeritics ASAP 2000 adsorption analyzer. Transient IR absorption signals were recorded on a Nicolet 870 FTIR spectrometer with a MCT detector. A pulse laser at 355 nm (1 Hz, 3 mJ per pulse) was used to excite the samples. The width of the laser pulse was 6–8 ns and no deconvolution on the data was carried out.

### Photocatalytic reactions

Photocatalytic reactions were carried out in a Pyrex top-irradiation type reaction vessel connected to a closed gas circulation system. Before photoirradiation, the reaction system was evacuated to completely remove air, and then irradiated from the top side using a 300 W xenon lamp with a filtration mirror equipped with an optical filter (Hoya, L-42;  $\lambda > 420$  nm) to cut off the ultraviolet light. A flow of cooling water was used to keep the reaction suspension at room temperature. Gas chromatography (Agilent; GC-7890A, MS-5A column, TCD, Ar carrier) was used to

analyze the evolved gases. The pH value before and after the photocatalytic overall water splitting reaction was similarly kept at *ca.* 6.

### Measurement of AQE

The AQE measurement was carried out using a Pyrex top-irradiation-type reaction vessel and a 300 W xenon lamp fitted with a 420 nm band-pass filter. The number of photons reaching the reaction solution was measured using a calibrated Si photodiode (LS-100, EKO Instruments Co., LTD.), and the AQE ( $\varphi$ ) was calculated according to the following equation:

$$\varphi(\%) = (AR/I) \times 100$$

where  $A$  represents a coefficient (4 for  $H_2$  evolution; 8 for  $O_2$  evolution),  $R$  represents the evolution rate of  $H_2$  or  $O_2$  in the initial one hour irradiation and  $I$  represents the absorption rate of incident photons. It was assumed that all incident photons were absorbed by the suspension. The total number of incident photons at a wavelength of 420 nm was measured to be  $4.76 \times 10^{20}$  photons per h.

## Results and discussion

Fig. 1A shows XRD patterns of the  $Ba(n)$ - $Ta_3N_5$  samples ( $n = 0-1$ ), in which all of them exhibit a well-crystallized feature. When the Ba/Ta molar ratio is below 0.03, only diffraction peaks assigned to a single phase of  $Ta_3N_5$  are observed. With a further enhanced molar ratio of Ba/Ta, additional diffraction peaks attributed to  $BaTaO_2N$  appear, the intensities of which are continuously increased. Compared with the diffraction peaks of the unmodified  $Ta_3N_5$  sample, a little shift in the diffraction peaks toward a lower angle is observed for the barium-modified  $Ta_3N_5$  samples (Fig. S1†). This demonstrates that the six-coordinated  $Ba^{2+}$  may be partly doped into  $Ta_3N_5$  to substitute the  $Ta^{5+}$  sites, similar to the previous report.<sup>30</sup>

Fig. 1B shows the UV-vis spectra of the  $Ba(n)$ - $Ta_3N_5$  samples, in which all of the samples similarly exhibit a wide visible light absorption at around 600 nm. The absorption edge is continuously red-shifted with the increasing molar ratio of Ba/Ta, which should be the result of the formed  $BaTaO_2N$  species. Compared to the pristine  $Ta_3N_5$  sample, the absorption background originating from the formation of reduced tantalum species (*e.g.*,  $Ta^{4+}$  and  $Ta^{3+}$ )<sup>43,44</sup> on the  $Ba(n)$ - $Ta_3N_5$  samples undergoes an initial decrease and a subsequent increase with the enhancing molar ratio of Ba/Ta. To understand the UV-Vis results, a single phase of  $BaTaO_2N$  was prepared *via* the same preparation procedure. As shown in Fig. 1B, the absorption edge of  $BaTaO_2N$  is at about 660 nm, and its absorption background is the highest among all of the  $Ta_3N_5$ -based samples. It is generally understood that the UV-vis absorption background of the mechanically mixed sample containing two phases should be located between that of the corresponding single phases. That is to say, if the  $Ba(n)$ - $Ta_3N_5$  samples are just a simple mixture of  $Ta_3N_5$  and  $BaTaO_2N$ , the absorption background of the  $Ba(n)$ - $Ta_3N_5$  samples will lie between those of the  $Ta_3N_5$  and  $BaTaO_2N$ . In this work, however, the samples with

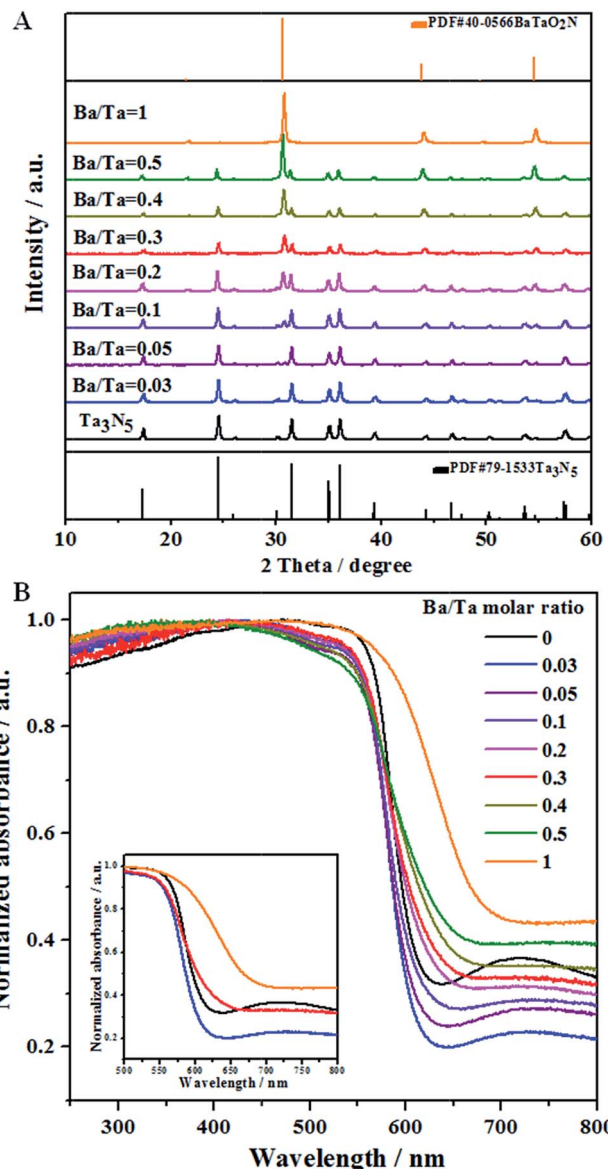


Fig. 1 Structural characterizations of typical  $Ba(n)$ - $Ta_3N_5$  samples ( $n = 0-1$ ): (A) XRD patterns and (B) UV-vis spectra. " $n$ " stands for the molar ratio of Ba/Ta. The inset figure is enlarged for the wavelength range of 500–800 nm.

a molar ratio of Ba/Ta below 0.3 exhibit much lower absorption backgrounds than those of both  $Ta_3N_5$  and  $BaTaO_2N$ . This means that the as obtained  $Ba(n)$ - $Ta_3N_5$  samples do not exist as a simple mixture of  $Ta_3N_5$  and  $BaTaO_2N$ , but exist as a nano-composite. In consideration of that, here the  $Ta_3N_5$  and  $BaTaO_2N$  phases are one-pot synthesized, thus the  $BaTaO_2N$  is expected to be formed *in situ* on the surface of  $Ta_3N_5$  to partly eliminate the surface dangling bonds of  $Ta_3N_5$ . On the other hand, the partial barium ions are doped into  $Ta_3N_5$  to inhibit the defect formation. Both of them cause the decrease of defect density. However, it needs to be pointed out that  $BaTaO_2N$  itself exhibits the highest defect density among all of the samples. Thus, when the molar ratio of Ba/Ta is excessively enhanced, the defect density of the  $Ba(n)$ - $Ta_3N_5$  sample will become higher



than that of  $Ta_3N_5$ . All of these factors should be integrally responsible for the initial decrease and subsequent increase of the absorption background (*i.e.* defect density) with the increasing molar ratio of Ba/Ta in the UV-Vis results (Fig. 1B).

Fig. 2 shows FESEM images of typical samples. The  $Ta_3N_5$  sample is porous (Fig. 2a), while the  $BaTaO_2N$  sample has a shortage of porosity (Fig. 2b). The difference in their morphology can be easily judged from their mixed sample (Fig. 2c). However, the morphology feature of the chosen  $Ba(0.3)-Ta_3N_5$  sample (Fig. 2d) prepared in this work is quite different from those of the corresponding single phases (Fig. 2a and b) or their mixed sample (Fig. 2c). As can be seen in Fig. 2d, the  $Ba(0.3)-Ta_3N_5$  sample exhibits a homogeneous morphology with the two phases difficult to distinguish, demonstrating their interaction with each other as a nanocomposite. The formation of the  $Ta_3N_5/BaTaO_2N$  nanocomposite can be further supported by the elemental mapping results (Fig. 2e-h). In Fig. 2f, the Ta element originating from both  $Ta_3N_5$  and  $BaTaO_2N$  is dispersed everywhere, while the Ba element that can only result from  $BaTaO_2N$  is only found in some specific places (Fig. 2g). This can be easily understood to show that the places with Ba element mapping mainly reveal the existence of  $BaTaO_2N$ , while the locations with Ta element mapping but a shortage of Ba element mapping stand for the  $Ta_3N_5$  species. Based on the elemental mapping images, we can reasonably give a simulation of the composite state of  $Ta_3N_5$  and  $BaTaO_2N$  for the  $Ba(0.3)-Ta_3N_5$  sample (Fig. 2h). For comparison, the element mapping results of mechanically mixed  $Ta_3N_5$  and  $BaTaO_2N$  ( $Ta_3N_5/BaTaO_2N$  (0.3)-mix) are given in Fig. S2,<sup>†</sup> from which the  $Ta_3N_5$  and  $BaTaO_2N$  phases are mainly separated, different from that of the  $Ba(0.3)-Ta_3N_5$  sample. It needs to be pointed out that the composite of  $Ta_3N_5$  and  $BaTaO_2N$  does not exist in a core-shell configuration. In addition, the surface areas of the  $Ba(n)-Ta_3N_5$  samples are similar to that of  $BaTaO_2N$  ( $7\text{ m}^2\text{ g}^{-1}$ ) but a little lower than that of  $Ta_3N_5$  ( $9\text{ m}^2\text{ g}^{-1}$ ), which should result from their shortage of porous structure (Table 1).

To further confirm the formation of the nanocomposite, we carried out a (HR)TEM characterization. Fig. 3 gives the

representative images of the  $Ba(0.3)-Ta_3N_5$  sample, in which the interface of the nanocomposite can be clearly observed. As shown in Fig. 3, the obvious lattice fringes indicate that the sample synthesized in this work is well-crystallized, in accordance with the XRD patterns (Fig. 1A). Based on the measurement of lattice distance, we can easily judge the  $BaTaO_2N$  and  $Ta_3N_5$  phases. Strikingly, the interfacial contact between  $BaTaO_2N$  and  $Ta_3N_5$  is very intimate, revealing the formation of the nanocomposite. The formation of the intimate interface should originate from the one-pot high temperature route and their similar Ta-based octahedron units. In this case,  $BaTaO_2N$  is expected to be formed *in situ* on the surface of  $Ta_3N_5$  during the one-pot nitridation process.

The relative band positions of  $Ta_3N_5$  and  $BaTaO_2N$  were analysed by combining their Mott-Schottky (M-S) plots and UV-Vis results. In Fig. 4a, the flat band potentials of  $BaTaO_2N$  and  $Ta_3N_5$  were evaluated according to M-S measurement results to be *ca.*  $-0.41\text{ V}$  and  $-0.32\text{ V}$  *vs.* NHE, respectively. In consideration of the fact that the bottom of the conduction band (CB) for one n-type semiconductor is normally more negative by *ca.*  $0.2\text{ V}$  than the flat band potential,<sup>24,45,46</sup> the CB positions of the n-type  $Ta_3N_5$  and  $BaTaO_2N$  are estimated to be  $-0.52\text{ eV}$  and  $-0.61\text{ eV}$ , respectively. By combining their bandgaps achieved from the UV-Vis results (Fig. 1B), the relative band positions of  $BaTaO_2N$  and  $Ta_3N_5$  are then deduced and given in Fig. 4b. Accordingly, the nanocomposite exists as a type II heterostructure, where the excited electrons are expected to transfer from the conduction band of  $BaTaO_2N$  to that of  $Ta_3N_5$ , while the photogenerated holes will transfer in an opposite way, leading to the spatial charge separation.

The photocatalytic  $H_2$  evolution rates on the pristine and modified  $Ta_3N_5$  samples were examined using the deposited platinum nanoparticle as the reduction cocatalyst in the presence of  $CH_3OH$  under visible light irradiation ( $\lambda > 420\text{ nm}$ ). No reaction takes place in the dark, and  $H_2$  is evolved only under light irradiation. As given in the half reaction part of Table 1, the rate of  $H_2$  evolution undergoes an initial increase and subsequent decrease with the increasing molar ratio of Ba/Ta, and the optimal value of the Ba/Ta molar ratio

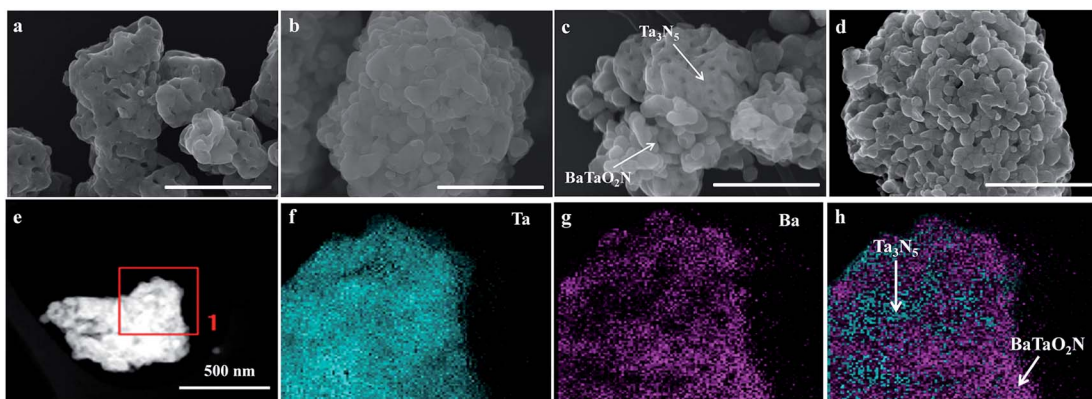


Fig. 2 FESEM images of typical samples: (a)  $Ta_3N_5$ , (b)  $BaTaO_2N$ , (c) a mixture of  $Ta_3N_5$  and  $BaTaO_2N$ , and (d)  $Ba(0.3)-Ta_3N_5$  (the scale bar is 500 nm). Elemental mappings of  $Ba(0.3)-Ta_3N_5$ : (e) TEM image, (f) Ta element, (g) Ba element, and (h) simulated dispersion of  $Ta_3N_5$  and  $BaTaO_2N$ .



Table 1 Photocatalytic performances of typical photocatalysts under visible light irradiation ( $\lambda > 420$  nm)

Entry	H <sub>2</sub> -evolving photocatalysts	Surface area (m <sup>2</sup> g <sup>-1</sup> )	H <sub>2</sub> evolution rate (μmol h <sup>-1</sup> )	Overall water splitting <sup>b</sup>	
				Half reaction <sup>a</sup>	
				Gas evolution rates (μmol h <sup>-1</sup> )	
1	Ba(0)-Ta <sub>3</sub> N <sub>5</sub>	9	0.05	0	0
2	Ba(0.03)-Ta <sub>3</sub> N <sub>5</sub>	7	0.1	Trace	Trace
3	Ba(0.05)-Ta <sub>3</sub> N <sub>5</sub>	7	4.2	0.8	0.4
4	Ba(0.1)-Ta <sub>3</sub> N <sub>5</sub>	7	6.6	2.0	1.0
5	Ba(0.2)-Ta <sub>3</sub> N <sub>5</sub>	7	19.3	2.5	1.3
6	Ba(0.3)-Ta <sub>3</sub> N <sub>5</sub>	7	30.2	3.2	1.6
7	Ba(0.4)-Ta <sub>3</sub> N <sub>5</sub>	7	28.2	3.0	1.5
8	Ba(0.5)-Ta <sub>3</sub> N <sub>5</sub>	7	24.6	2.1	1.1
9	BaTaO <sub>2</sub> N	7	9.5	0.3	0.15
10	Ta <sub>3</sub> N <sub>5</sub> /BaTaO <sub>2</sub> N (0.3)-mix	8	16.5	0.6	0.3

<sup>a</sup> Reaction conditions: 0.15 g of 0.5 wt% Pt/Ba(*n*)-Ta<sub>3</sub>N<sub>5</sub> (*n* = 0–1) and 0.5 wt% Pt/Ta<sub>3</sub>N<sub>5</sub>/BaTaO<sub>2</sub>N (0.3)-mix samples; 0.15 g of La<sub>2</sub>O<sub>3</sub>; aqueous methanol solution (150 mL, 20 vol%); 300 W xenon lamp ( $\lambda > 420$  nm); 1 h irradiation. <sup>b</sup> Reaction conditions: 50 mg of 0.5 wt% Pt-modified H<sub>2</sub>-evolving photocatalysts; 50 mg of 0.45 wt% PtO<sub>x</sub>/WO<sub>3</sub> as O<sub>2</sub>-evolving photocatalyst; 100 mL of aqueous NaI solution (1.0 mM); Pyrex top-irradiation type; 300 W xenon lamp ( $\lambda > 420$  nm); 1 h irradiation.

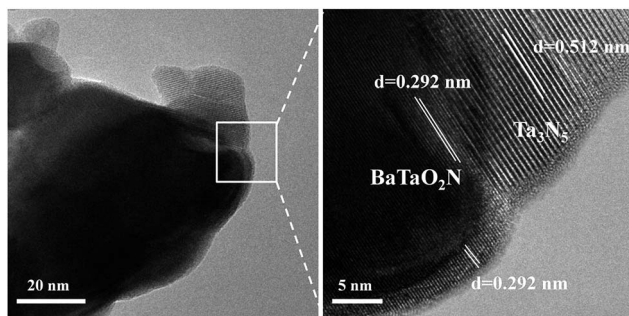


Fig. 3 Representative TEM (left) and locally enlarged HRTEM (right) images of the chosen Ba(0.3)-Ta<sub>3</sub>N<sub>5</sub> sample.

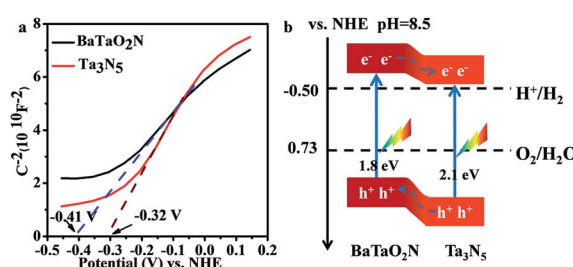


Fig. 4 Band structure characterizations of the Ta<sub>3</sub>N<sub>5</sub> and BaTaO<sub>2</sub>N samples. (a) Mott-Schottky plot for the Ta<sub>3</sub>N<sub>5</sub> and BaTaO<sub>2</sub>N electrodes. Electrolyte: 0.5 M Na<sub>2</sub>SO<sub>4</sub> solution (pH = 8.5, adjusted using NaOH). Frequency: 1000 Hz. (b) The relative band positions of the Ta<sub>3</sub>N<sub>5</sub>/BaTaO<sub>2</sub>N heterostructure.

is 0.3. Compared to the Ta<sub>3</sub>N<sub>5</sub> (entry 1), BaTaO<sub>2</sub>N (entry 9) or Ta<sub>3</sub>N<sub>5</sub>/BaTaO<sub>2</sub>N (0.3)-mix (entry 10) sample, the H<sub>2</sub> evolution rate on the Pt/Ba(0.3)-Ta<sub>3</sub>N<sub>5</sub> photocatalyst is remarkably promoted. The typical time curve of H<sub>2</sub> evolution on the Pt/

Ba(0.3)-Ta<sub>3</sub>N<sub>5</sub> sample is given in Fig. S3,† in which it is almost linearly increased in the experimental region, demonstrating its good photochemical stability. In addition, only a small amount of N<sub>2</sub> (less than 1 μmol) was detected in the initial stage of irradiation. The dependence of the H<sub>2</sub> evolution rate on the Pt/Ba(0.3)-Ta<sub>3</sub>N<sub>5</sub> photocatalyst as a function of irradiation wavelength is well consistent with that of the UV-vis spectra (Fig. S4†), indicating that the H<sub>2</sub> evolution process is driven by the incident light.

Encouraged by the significantly enhanced H<sub>2</sub> evolution rate, we tried to use the pristine or barium-modified Ta<sub>3</sub>N<sub>5</sub> samples as H<sub>2</sub>-evolving photocatalysts to construct a Z-scheme overall water splitting system together with a PtO<sub>x</sub>/WO<sub>3</sub> and IO<sub>3</sub><sup>-</sup>/I<sup>-</sup> pair as an O<sub>2</sub>-evolving photocatalyst and redox mediator, respectively. As shown in the overall water splitting part of Table 1, when using pristine Ta<sub>3</sub>N<sub>5</sub> as the H<sub>2</sub>-evolving photocatalyst (entry 1), no obvious H<sub>2</sub> evolution is detected, demonstrating the infeasibility of Ta<sub>3</sub>N<sub>5</sub> itself to drive the Z-scheme overall water splitting process. However, using the barium-modified Ta<sub>3</sub>N<sub>5</sub> samples as H<sub>2</sub>-evolving photocatalysts (entries 2–8), overall water splitting with H<sub>2</sub>/O<sub>2</sub> molar ratios of close to 2 : 1 is achieved, and the photocatalytic activity is dependent on the Ba/Ta molar ratio with an optimal value of *ca.* 0.3. The Z-scheme activities using the barium-modified samples as H<sub>2</sub>-evolving photocatalysts (entries 2–8) are all higher than those using BaTaO<sub>2</sub>N (entry 9) or the mixed sample (entry 10). The AQE was measured using the Ba(0.3)-Ta<sub>3</sub>N<sub>5</sub> sample as the H<sub>2</sub>-evolving photocatalyst to be 0.1% at 420 nm. The activity trend is similar to the result of the photocatalytic proton reduction reaction, indicating that the overall water splitting performance is rate-determined by the H<sub>2</sub>-evolving side. In addition, the multiple cycles of time course curves further demonstrate its photochemical stability in the experimental region (Fig. 5). No obvious Ba<sup>2+</sup> ion residue is observed in the centrifuged solution after reaction.

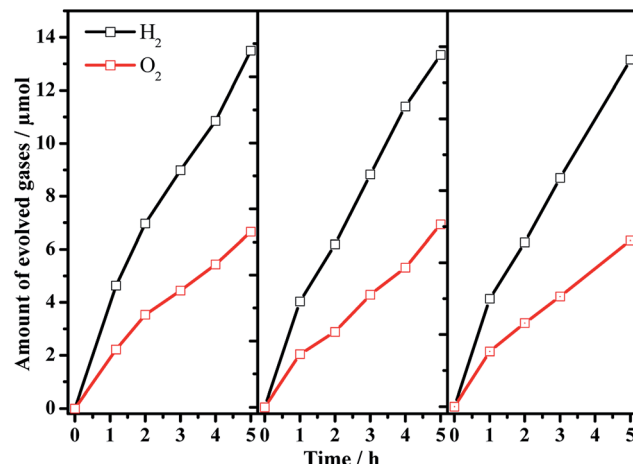


Fig. 5 Multiple cycles of Z-scheme overall water splitting with 0.5 wt% Pt/Ba(0.3)-Ta<sub>3</sub>N<sub>5</sub> and 0.45 wt% PtO<sub>x</sub>/WO<sub>3</sub> as H<sub>2</sub>-evolving and O<sub>2</sub>-evolving photocatalysts, respectively. Reaction conditions: 50 mg of Pt/Ba(0.3)-Ta<sub>3</sub>N<sub>5</sub> and 50 mg of PtO<sub>x</sub>/WO<sub>3</sub>; 100 mL of NaI aqueous solution (1.0 mM); 300 W xenon lamp ( $\lambda > 420$  nm), top-irradiation.

Photocatalytic overall water splitting commonly confronts huge challenges from both thermodynamic and kinetic aspects.<sup>2,47</sup> In the past few decades, many candidate materials have satisfied the thermodynamics requirement, but overall water splitting on them is unfeasible because of the constraint of insufficient reaction kinetics in the H<sub>2</sub> and/or O<sub>2</sub>-evolving side. Accordingly, developing strategies to address the water splitting reaction kinetics, which is greatly affected by the charge separation and surface catalytic process, is highly valuable. In this work, we adopt a simple one-pot nitridation approach with an ammonia flow (250 mL min<sup>-1</sup>) at high temperature (1223 K) to address the key issue of the charge separation *via* barium modification of Ta<sub>3</sub>N<sub>5</sub>. Based on our modification, not only is the defect density of Ta<sub>3</sub>N<sub>5</sub> decreased, but also a Ta<sub>3</sub>N<sub>5</sub>/BaTaO<sub>2</sub>N heterostructure with intimate interfacial contact is formed for the promotion of spatial charge separation. Both of these are reasonably responsible for promoting photogenerated charge separation, contributing to the enhanced proton reduction performance as well as the feasible overall water splitting process. The promotion of charge separation is confirmed by comparing the time-resolved infrared spectra (TRIR) of the typical Ta<sub>3</sub>N<sub>5</sub>, BaTaO<sub>2</sub>N and Ba(0.3)-Ta<sub>3</sub>N<sub>5</sub> samples (Fig. 6). The effective formation of the Ta<sub>3</sub>N<sub>5</sub>/BaTaO<sub>2</sub>N heterostructure probably originates from their similar structure units containing Ta-based octahedra. The decreased defect density of Ta<sub>3</sub>N<sub>5</sub> originates from the part doping of Ba ions and the formation of BaTaO<sub>2</sub>N on the surface of Ta<sub>3</sub>N<sub>5</sub> leading to surface passivation. It needs to be pointed out that with the increasing Ba/Ta molar ratio, the content of BaTaO<sub>2</sub>N with the highest defect density (see UV-Vis results in Fig. 1B) is enhanced, resulting in the increase of recombination centres, which is unfavourable for the photocatalytic H<sub>2</sub> evolution process. As an integral factor of the heterostructure and the defect centres, the photocatalytic activity exhibits an initial increase and a subsequent decrease with the increasing molar ratio of Ba/Ta.

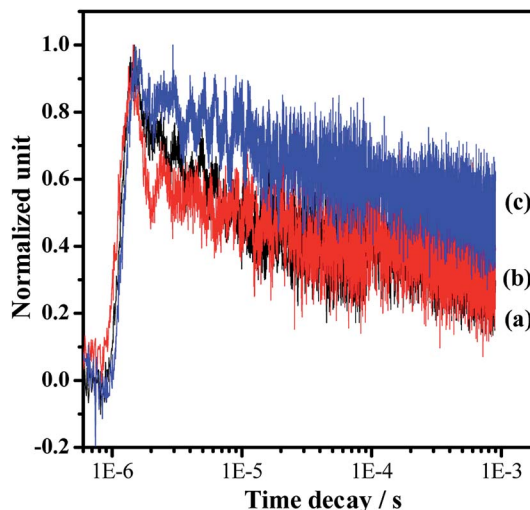


Fig. 6 Normalized transient absorption profiles of the representative samples in a vacuum: (a) Pt/Ta<sub>3</sub>N<sub>5</sub>, (b) Pt/BaTaO<sub>2</sub>N and (c) Pt/Ba(0.3)-Ta<sub>3</sub>N<sub>5</sub>. The pulse laser at 355 nm was used to excite the samples for the IR tests. The cocatalyst of Pt with a loading amount of 0.5 wt% was deposited by impregnation and a subsequent H<sub>2</sub> reduction method.

## Conclusions

In summary, a simple one-pot nitridation strategy is adopted for the barium modification of Ta<sub>3</sub>N<sub>5</sub> photocatalyst to address its poor photogenerated carrier separation ability as well as H<sub>2</sub>-evolving activity. The one-pot nitridation route overcomes well the challenge of low thermal stability in air for (oxy)nitride-related photocatalysts. Based on this, barium ions are partially doped into Ta<sub>3</sub>N<sub>5</sub> to inhibit the formation of defects, and the residue amount of barium ions will cause the *in situ* formation of BaTaO<sub>2</sub>N on the surface of Ta<sub>3</sub>N<sub>5</sub> to create an intimate interface for the Ta<sub>3</sub>N<sub>5</sub>/BaTaO<sub>2</sub>N heterostructure. Both of the structures favour the enhancement of charge separation efficiency as well as the promotion of the H<sub>2</sub>-evolving rate. Finally, we successfully achieve a Z-scheme overall water splitting process under visible light irradiation using the Ba-modified Ta<sub>3</sub>N<sub>5</sub> as a H<sub>2</sub>-evolving photocatalyst. The fabrication of the heterostructure *via* a one-pot route is expected to be extended into more (oxy)nitride systems for promoted solar energy conversion.

## Acknowledgements

This work was financially supported by the Basic Research Program of China (973 Program: 2014CB239403) and National Natural Science Foundation of China (21373210, 21522306). F. Zhang thanks the “Hundred Talents Program” of Chinese Academy of Sciences for the preferential support.

## Notes and references

- 1 K. Maeda and K. Domen, *J. Phys. Chem. C*, 2007, **111**, 7851–7861.
- 2 A. Kudo and Y. Miseki, *Chem. Soc. Rev.*, 2009, **38**, 253–278.



3 R. Abe, *J. Photochem. Photobiol. C*, 2010, **11**, 179–209.

4 X. Zong and L. Z. Wang, *J. Photochem. Photobiol. C*, 2014, **18**, 32–49.

5 D. M. Fabian, S. Hu, N. Singh, F. A. Houle, T. Hisatomi, K. Domen, F. E. Osterloh and S. Ardo, *Energy Environ. Sci.*, 2015, **8**, 2825–2850.

6 F. E. Osterloh, *Chem. Mater.*, 2008, **20**, 35–54.

7 H. Tong, S. X. Ouyang, Y. P. Bi, N. Umezawa, M. Oshikiri and J. H. Ye, *Adv. Mater.*, 2012, **24**, 229–251.

8 X. B. Chen, S. H. Shen, L. J. Guo and S. S. Mao, *Chem. Rev.*, 2010, **110**, 6503–6570.

9 Y. Wang, X. C. Wang and M. Antonietti, *Angew. Chem., Int. Ed.*, 2012, **51**, 68–89.

10 Y. Ma, X. L. Wang, Y. S. Jia, X. B. Chen, H. X. Han and C. Li, *Chem. Rev.*, 2014, **114**, 9987–10043.

11 K. Maeda, K. Teramura, D. L. Lu, T. Takata, N. Saito, Y. Inoue and K. Domen, *Nature*, 2006, **440**, 295.

12 Y. Sasaki, H. Kato and A. Kudo, *J. Am. Chem. Soc.*, 2013, **135**, 5441–5449.

13 W. Y. Wang, J. Chen, C. Li and W. M. Tian, *Nat. Commun.*, 2014, **5**, 4647.

14 C. S. Pan, T. Takata, M. Nakabayashi, T. Matsumoto, N. Shibata, Y. Ikuhara and K. Domen, *Angew. Chem., Int. Ed.*, 2015, **54**, 2955–2959.

15 Q. X. Jia, A. Iwase and A. Kudo, *Chem. Sci.*, 2014, **5**, 1513–1519.

16 S. S. Chen, Y. Qi, T. Hisatomi, Q. Ding, T. Asai, Z. Li, S. S. K. Ma, F. X. Zhang, K. Domen and C. Li, *Angew. Chem., Int. Ed.*, 2015, **54**, 8498–8501.

17 D. J. Martin, P. J. T. Reardon, S. J. A. Moniz and J. W. Tang, *J. Am. Chem. Soc.*, 2014, **136**, 12568–12571.

18 G. G. Zhang, Z. A. Lan, L. H. Lin, S. Lin and X. C. Wang, *Chem. Sci.*, 2016, **7**, 3062–3066.

19 G. Hitoki, A. Ishikawa, T. Takata, J. N. Kondo, M. Hara and K. Domen, *Chem. Lett.*, 2002, 736–737.

20 A. Ishikawa, T. Takata, J. N. Kondo, M. Hara and K. Domen, *J. Phys. Chem. B*, 2004, **108**, 11049–11053.

21 A. B. Murphy, P. R. F. Barnes, L. K. Randeniya, I. C. Plumb, I. E. Grey, M. D. Horne and J. A. Glasscock, *Int. J. Hydrogen Energy*, 2006, **31**, 1999–2017.

22 S. S. K. Ma, T. Hisatomi, K. Maeda, Y. Moriya and K. Domen, *J. Am. Chem. Soc.*, 2012, **134**, 19993–19996.

23 Z. Wang, J. G. Hou, S. Q. Jiao, K. Huang and H. Zhu, *J. Mater. Chem.*, 2012, **22**, 21972–21978.

24 S. S. Chen, G. J. Liu, Y. Qi, F. X. Zhang and C. Li, *Angew. Chem., Int. Ed.*, 2015, **54**, 3047–3051.

25 M. Tabata, K. Maeda, M. Higashi, D. L. Lu, T. Takata, R. Abe and K. Domen, *Langmuir*, 2010, **26**, 9161–9165.

26 M. J. Liao, J. Y. Feng, W. J. Luo, Z. Q. Wang, J. Y. Zhang, Z. S. Li, T. Yu and Z. Z. Zou, *Adv. Funct. Mater.*, 2012, **22**, 3066–3074.

27 G. J. Liu, J. Y. Shi, F. X. Zhang, Z. Chen, J. F. Han, C. M. Ding, S. S. Chen, Z. L. Wang, H. X. Han and C. Li, *Angew. Chem., Int. Ed.*, 2014, **53**, 7295–7299.

28 L. Wang, N. T. Nguyen, X. M. Zhou, I. Hwang, M. S. Killian and P. Schmuki, *ChemSusChem*, 2015, **8**, 2615–2620.

29 J. Seo, T. Takata, M. Nakabayashi, T. Hisatomi, N. Shibata, T. Minegishi and K. Domen, *J. Am. Chem. Soc.*, 2015, **137**, 12780–12783.

30 Y. B. Li, L. Zhang, A. Torres-Pardo, J. M. Gonzalez-Calbet, Y. H. Ma, P. Oleynikov, O. Terasaki, S. Asahina, M. Shima, D. Cha, L. Zhao, K. Takanabe, J. Kubota and K. Domen, *Nat. Commun.*, 2013, **4**, 2566.

31 G. J. Liu, S. Ye, P. L. Yan, F. Q. Xiong, P. Fu, Z. L. Wang, Z. Chen, J. Y. Shi and C. Li, *Energy Environ. Sci.*, 2016, **9**, 1327–1334.

32 M. Y. Tsang, N. E. Pridmore, L. J. Gillie, Y. H. Chou, R. Brydson and R. E. Douthwaite, *Adv. Mater.*, 2012, **24**, 3406–3409.

33 L. Yuliati, J. H. Yang, X. C. Wang, K. Maeda, T. Takata, M. Antonietti and K. Domen, *J. Mater. Chem.*, 2010, **20**, 4295–4299.

34 K. Maeda, N. Nishimura and K. Domen, *Appl. Catal., A*, 2009, **370**, 88–92.

35 D. A. Wang, T. Hisatomi, T. Takata, C. S. Pan, M. Katayama, J. Kubota and K. Domen, *Angew. Chem., Int. Ed.*, 2013, **52**, 11252–11256.

36 X. M. Liu, L. Zhao, K. Domen and K. Takanabe, *Mater. Res. Bull.*, 2014, **49**, 58–65.

37 S. S. Chen, Y. Qi, Q. Ding, Z. Li, J. Y. Cui, F. X. Zhang and C. Li, *J. Catal.*, 2016, **339**, 77–83.

38 V. Strahle, *Z. Anorg. Allg. Chem.*, 1973, **402**, 47–57.

39 J. Zhang, Q. Xu, Z. C. Feng, M. J. Li and C. Li, *Angew. Chem., Int. Ed.*, 2008, **47**, 1766–1769.

40 X. Wang, Q. Xu, M. R. Li, S. Shen, X. L. Wang, Y. C. Wang, Z. C. Feng, Y. S. Shi, H. X. Han and C. Li, *Angew. Chem., Int. Ed.*, 2012, **51**, 13089–13092.

41 J. Z. Su, L. J. Cuo, N. Z. Bao and C. A. Grimes, *Nano Lett.*, 2011, **11**, 1928–1933.

42 E. S. Kim, N. Nishimura, G. Magesh, J. Y. Kim, J. W. Jang, H. Jun, J. Kubota, K. Domen and J. S. Lee, *J. Am. Chem. Soc.*, 2013, **135**, 5375–5383.

43 J. Q. Wang, S. Y. Su, B. Liu, M. H. Cao and C. W. Hu, *Chem. Commun.*, 2013, **49**, 7830–7832.

44 K. Maeda, M. Higashi, D. L. Lu, R. Abe and K. Domen, *J. Am. Chem. Soc.*, 2010, **132**, 5858–5868.

45 Y. Matsumoto, *J. Solid State Chem.*, 1996, **126**, 227–234.

46 S. S. Chen, Q. Yi, G. J. Liu, J. X. Yang, F. X. Zhang and C. Li, *Chem. Commun.*, 2014, **50**, 14415–14417.

47 T. Hisatomi, J. Kubota and K. Domen, *Chem. Soc. Rev.*, 2014, **43**, 7520–7535.

